Acta Geotechnica
https://doi.org/10.1007/s11440-024-02456-z

RESEARCH PAPER

Resistive force modeling for shallow cone penetration into dry and wet granular layers

Naoki Iikawa[1,2,3] · Hiroaki Katsuragi[1]

Received: 20 February 2024 / Accepted: 2 November 2024

Abstract

Estimating penetration resistive forces on granular materials is important for applications in various research fields. This paper investigates resistive forces into dry and wet granular layers through theoretical analysis and discrete element simulations. Theoretical model is derived from slip line field theory by assuming materials with cohesion and inter-particle friction. This model indicates that penetration resistive forces are composed of the sum of the buoyancy-like force proportional to the penetration volume and the cohesion-derived force proportional to the penetration cross-sectional area. The model is compared with the simulation results of various cones shallowly penetrating into granular layers with/without liquid-bridge forces between particles. For cohesion-derived force, the simulated resistive forces agree with the theoretical model within a factor of two. For buoyancy-like force, on the other hand, the simulated resistive forces deviate from the theoretical model by up to five times as the cone-tip angle increased. To solve the discrepancy, this paper introduces the correction factor depending on the relationship between stagnant zone and cone shape. As a result, a maximum difference between the proposed model and simulated force are reduced to twice. Thereby, it turns out that the proposed model can compute penetration resistive forces on granular layers in a wide range of cone-tip angles and water content conditions.

Keywords Discrete element modeling · Granular materials · Shallow cone penetration · Stress analysis

List of symbols

β	Tip angle of stagnant zone
χ	Shape parameter of particle
Δx	Coefficient of distance which the cohesive force continues after particles detouch
$\delta_{\theta ri}$, $\delta_{\theta si}$	Total relative rolling and twisting angular displacements from particle j to i
$\delta_{\theta ri}$, $\delta_{\theta si}$	Total relative rolling and twisting angular displacements from particle j to i
δ_{nij}, δ_{tij}	Normal and tangential displacements between particles i and j [m]
γ_n, γ_t	Normal and tangential viscous dampings [kg/s]
μ	Sliding friction coefficient
μ_{gg}	Sliding friction coefficient between particles
μ_{og}	Sliding friction coefficient between cone and particle
ω_i	Angular velocity of particle i [s^{-1}]
ω_{ri}, ω_{si}	Relative rolling and twisting angular velocities from particles j to i [s^{-1}]
ϕ	Internal friction angle [deg]
ρ_g, ρ_o	Densities of particle and cone [kg/m^3]
Θ	Tip angle of cone [deg]
ξ	Coefficient to caluculate γ_n and γ_t
C	Cohesive stress parameter in DEM [Pa]
C'	Cohesive stress in the Mohr–Coulomb's yield criterion [Pa]
E^*	Effective Young's modulus [Pa]
$f(\Theta)$	Correction factor for Θ
F_c^j	Liquid-bridge force from adjacent particle j [N]
F_n^j,F_t^j	Normal and tangential forces between particles i and j [N]
F_C	Liquid-bridge-derived penetration resistive force [N]

✉ Naoki Iikawa
naoki_iikawa@global.komatsu

Hiroaki Katsuragi
katsuragi@ess.sci.osaka-u.ac.jp

[1] Department of Earth and Space Science, Osaka University, 1-1 Machikaneyama, Toyonaka, Osaka 560-0043, Japan

[2] Development Division, Komatsu Ltd, 3-25-1 Shinomiya, Hiratsuka, Kanagawa 254-8555, Japan

[3] Komatsu MIRAI Construction Equipment Cooperative Research Center, Osaka University, 1-1 Yamadaoka, Suita, Osaka 565-0871, Japan

Published online: 03 December 2024

F_{dry}, F_{wet}	Penetration resistive forces in dry and wet condition [N]
g	Gravitational acceleration [m/s^2]
G^*	Effective shear modulus [Pa]
I_i	Moment of inertia of particle i [kg/m^2]
k_n, k_t	Normal and tangential spring constants [kg/s^2]
K_c, K_ϕ	Coefficients of cohesion-derived and buoyancy-like forces
m^*	Effective mass [kg]
m_i	Mass of particle i [kg]
M_r^j, M_s^j	Rolling and twisting moments from particle j to i [Nm]
R	Radius of cone [m]
r^*	Effective radius [m]
r_i, r_j	Radii of particle i and j [m]
r_i^j	Vector from the center of particle i to the contact point with particle j [m]
R_p	Penetrated radius of cone [m]
S_n, S_t	Coefficients to calculate γ_n and γ_t
t	Time [s]
T_R	Rayleigh time [s]
v_i	Velocity of particle i [m/s]
V_p	Penetration volume of a intruder [mm^3]
v_{nij}, v_{tij}	Normal and tangential relative velocities from particle i to j [m/s]
x, y, z	Axis in Cartesian coordinates
z_p	Penetration depth [mm]

1 Introduction

The surfaces of the Earth and several other solid planets are composed of granular materials. On these surfaces, many activities of machines and living organisms (animals and plants), such as landing [5], locomotion [40], and excavation [21], daily take place. These phenomena vary in behavior but are in common that these occur when objects penetrate into granular layer. Thereby, for applications in many fields, it is important to estimate the resistive force exerting on the penetrating object.

Various models have been proposed to estimate resistive force that an intruder vertically penetrates into granular layer. In Geotechnical Engineering, the theoretical models have been developed by considering the soil ground as a rigid-plastic body and applying the slip line field theory [24, 27]. These theoretical models are applied in combination with empirically and computationally derived coefficients to calculate such as bearing capacity of foundations on soil ground. In other areas, the phenomenological models mainly for shallow penetration (at a depth of 2–5 times the intruder's diameter) have been also proposed. These models are often expressed as the sum of a depth-dependent term derived from buoyancy-like pressure and a velocity-dependent term derived from viscosity and inertia [8, 9, 19]. In Planetary Science, these models are used to investigate the dynamics of impact crater and the mechanical properties of regolith [10, 18, 32]. In Biology, these models are used to comprehend the ecology and morphology of plants and animals on sand [7, 26, 28, 39]. In Terramechanics, as an application of these phenomenological models, granular resistive force theory (RFT) has been developed [3, 25]. RFT calibrates the resistive force resulting from the combination of inclination and direction of penetration of a small area relative to the granular layer in advance. Following the calibrated parameter, it calculates the resistive force for each minute intruder's surface area in contact with the granular layer. This method enables accurate estimation of the resistive force. In fact, simulations have been performed to reproduce the behaviors of robots and tires on granular layer by combining with RFT and multi-body dynamics [1, 25, 40].

Among these previous studies, on the basis of the above classical theories in Geotechnical Engineering, a new model is proposed recently [11, 17]. This model is called as modified Archimedes' law theory (MALT) and described as follows:

$$F_{dry}(z_p) = K_\phi \rho_g \psi g V_p(z_p), \tag{1}$$

$$\text{with} \quad K_\phi \equiv \left(2\frac{1+\sin\phi}{1-\sin\phi} e^{\pi \tan\phi} \int_0^1 \eta A(\eta,\phi) d\eta \right), \quad \text{where}$$

F_{dry} is the resistive force on an intruder vertically penetrating the dry granular layer; z_p and $V_p(z_p)$ are the penetration depth and the penetration volume of an intruder, respectively; ρ_g and g are density of granular particles and the gravitational acceleration ($g = 9.8$ m/s^2), respectively; ψ is packing fraction which is the value obtained by subtracting the porosity from 1; and K_ϕ is a coefficient which depends only on the internal friction angle of granular materials, ϕ. The details of parameters η and $A(\eta, \phi)$ in MALT are explained in Appendix A. Compared with RFT, MALT can not provide detailed stresses distribution applied to each surface of the intruder. On the other hand, MALT does not require a prior calibration as in RFT. Therefore, it is suitable for estimating the soil properties of unknown granular materials or for calculating resistive forces only from ϕ. Because of its simplicity, MALT has been used in various studies related to shallow penetrations [10, 37].

However, there are several issues in applying MALT for machines and living organisms. The first issue is the effect of the intruder shape. Kang et al [17] have validated MALT with respect to various geometries such as cylinders, spheres, and cones, but only for cone-tip angles close to ϕ. On the other hand, Mishra et al [28]; Tovar-Valencia Ruben D. et al [44]; and Hunt et al [13] have reported that a sharp tip on cones of the same diameter reduces penetration resistances at shallow depths. Focusing only on the tip, same radius cones generally have larger height and volume with sharp tip angles. Thus, MALT might not explain cone-tip angle dependence on penetration resistive forces. The second issue is the consideration of cohesion in granular materials. As is clear from Eq. (1), MALT does not consider the cohesion effect due to clay and liquid bridge between particles. However, in natural state on the Earth, water is often contained between particles in granular materials. Thus, it is important in applications to consider F_{wet} (the penetration resistive force in wet granular materials which liquid-bridge force exists between particles by adding water). In fact, F_{wet} has been investigated in Terramechanics and Biological application studies [4, 39]. Although these previous studies have qualitatively shown that F_{wet} increases as the moisture content becomes large, these results are not sufficient for quantitative estimation. Therefore, F_{wet} needs to be quantitatively investigated and modeled for application to realistic phenomena.

To address the above issues, this study investigates the effects of cone-tip angle and liquid-bridge forces in wet granular materials on resistive forces at shallow penetration. Firstly, the effect of cone-tip angle to F_{dry} is investigated and discussed from discrete element method (DEM) simulations. Furthermore, to explain F_{dry} for various cone angles calculated by DEM simulation, this study proposes a correction of MALT according to the cone-tip angle. Secondly, in order to construct a model to calculate F_{wet}, this study extends MALT to the model where cohesive forces between particles are considered by assuming a Mohr–Coulomb's yield criterion with a cohesive stress term. The consistency of the derived model is confirmed by comparing it with obtained F_{wet} from DEM simulations when liquid-bridge force is added between particles. Therefore, this study indicates that the model combining above two results can explain the resistive force for shallow cone penetration with various tip angles into dry and wet granular layers.

2 Methods

2.1 Discrete element method (DEM)

To perform the discrete element simulations, an open-source DEM engine, LIGGGHTS(R)-PUBLIC Version 3.8.0 [6, 20] is used. In the simulations, to reproduce the behavior of dry and wet granular materials, the Hertz–Mindlin contact model, the rolling resistance model [2, 16], and cohesive bond force model [45, 46] are employed, respectively. These choices are based on the previous studies [31, 45]. To be specific, these previous studies have reported that a combination of linear spring and cohesive bond force models can reproduce the bulk response of wet glass beads and sandy soils, independent of the presence or absence of a rotational resistance model. Thus, the models used in this study should be able to reproduce the response of wet glass beads and sand in the penduler regime.

The equations of motion for the translational and rotational directions of the particle i are expressed by the following equations:

$$\begin{aligned} m_i \frac{dv_i}{dt} &= \sum (F_n^j + F_t^j + F_c^j) + m_i g, \\ I_i \frac{d\omega_i}{dt} &= \sum (r_i^j \times F_t^j + M_r^j + M_s^j), \end{aligned} \tag{2}$$

where m_i, v_i, I_i, and ω_i represent the mass, translational velocity, moment of inertia, and angular velocity of particle i, respectively; F_n^j and F_t^j represent the normal and tangential forces between contacting particles i and j, respectively; F_c^j represents the liquid-bridge force from adjacent particle j to particle i; r_i^j is the vector from the center of particle i to the contact point with particle j; and M_r^j and M_s^j represent the rolling and twisting moments from contacting particle j to particle i due to rolling resistance, respectively. The symbol $\sum$ denotes the sum of all forces or moments acting on particle i from adjacent particles.

F_n^j and F_t^j in Eq. (2) fully follow the Hertz model in LIGGGHTS. Each force is described as follows:

$$\begin{aligned} F_n^j &= k_n \delta_{nij} + \gamma_n v_{nij}, \\ F_t^j &= \min[\mu |F_n^j|, k_t \delta_{tij} + \gamma_t v_{tij}], \end{aligned} \tag{3}$$

where δ_{nij} and δ_{tij} are the normal and tangential displacements between contacting particles i and j, respectively; v_{nij} and v_{tij} are the normal and tangential relative velocities from contacting particle j to particle i, respectively; μ represents the sliding friction coefficient; μ_{gg} is used between particles and μ_{og} between cone and particle, respectively. The symbol "min" denotes choice of the smaller of the two values in parentheses. k_n, k_t, γ_n, and γ_t

are the normal spring constant, the tangential spring constant, the normal viscous damping coefficient, and the tangential viscous damping coefficient, respectively. Here, k_n, k_t, γ_n, and γ_t are defined as follows:

$$\begin{aligned} k_n &= \frac{4}{3}E^*\sqrt{r^*\delta_{nij}}, \\ k_t &= 8G^*\sqrt{r^*\delta_{nij}}, \\ \gamma_n &= 2\sqrt{\frac{5}{6}}\xi\sqrt{S_n m^*}, \\ \gamma_t &= 2\sqrt{\frac{5}{6}}\xi\sqrt{S_t m^*}, \end{aligned} \tag{4}$$

where S_n and S_t are defined as $S_n = 2E^*\sqrt{r^*\delta_{nij}}$, $S_t = 8\,G^*\sqrt{r^*\delta_{nij}}$, respectively. The effective radius r^*, the effective mass m^*, the effective Young's modulus E^*, and the effective shear modulus G^* are, respectively, calculated from each physical quantity of contacting particles i and j. Using the coefficient of restitution e which is the ratio of the relative velocities of two particles before and after a collision, the parameter ξ is defined as follows: $\xi = \frac{\ln(e)}{\sqrt{\ln^2(e)+\pi^2}}$.

M_r^j and M_s^j in Eq. (2) also fully follow the rolling resistance model proposed by Jiang et al [16]. Each moment is described as follows:

$$\begin{aligned} M_r^j &= \min\left[0.525|F_n^j|\chi r^*,\ 0.25(\chi r^*)^2(k_n\delta_{\theta ri} + \gamma_n\omega_{ri})\right], \\ M_s^j &= \min\left[0.65\mu|F_n^j|\chi r^*,\ 0.5(\chi r^*)^2(k_t\delta_{\theta si} + \gamma_t\omega_{si})\right], \end{aligned} \tag{5}$$

where $\delta_{\theta ri}$, $\delta_{\theta si}$, ω_{ri}, and ω_{si} are the total relative rolling angular displacement, the total relative twisting angular displacement, the relative rolling angular velocity, and the relative twisting angular velocity, in the contact of particles i and j, respectively. χ is a dimensionless shape parameter that adjusts the rotational resistance force due to the irregularity of the actual particle shape. The closer the actual particle shape is to a true sphere, the closer to zero it is. Coefficient values in Eq. (5) are taken directly from the values determined by Jiang et al [16].

F_c^j in Eq. (2) basically follows the cohesive bond force model proposed by Tsuji et al [45, 46]. This model is built from an analogy to the macroscopic shear failure characteristics of cohesive soil. In this model, the attraction force only acts between contacted particles i and j, and is described as follows:

$$F_c^j = \begin{cases} -\dfrac{C}{\mu_{gg}}(r_i + r_j)^2 & : \text{if } \delta_{nij} \geq 0, \\ -\dfrac{C}{\mu_{gg}}(r_i + r_j)^2\left(1 - \dfrac{|x_i - x_j| - (r_i + r_j)}{\Delta x(r_i + r_j)}\right) & : \text{if } \delta_{nij} < 0, \text{ separation}, \\ 0 & : \text{if } \delta_{nij} < 0, \text{ approach}, \end{cases} \tag{6}$$

where C is the attraction stress parameter that represents the degree of liquid-bridge force between particles i and j. Here, C is proportional to liquid-bridge force, and μ_{gg} is inversely proportional in Eq. (6). The reason is that the intersection of the Mohr–Coulomb's yield criterion and the normal stress axis is equal to $\frac{C}{\mu_{gg}}$ as reported by Mitarai and Nori [29]. The distance until which the liquid bridge continues after particles detouching is set as $\Delta x = 0.1$ times the mean diameter of contacted particles i and j, as in Tsuji et al [46]. On the other hand, Eq. (6) differs from Tsuji et al [45, 46] in that it includes particle size dependence. In these previous studies, DEM simulation is calculated with a single-particle diameter, whereas in this study, multiple particle sizes are included to avoid particle crystallization [14]. For this reason, the liquid-bridge force is given as proportional to the square of the mean diameter of the contacted particles i and j.

2.2 Parameter calibration

The DEM parameters are determined by comparing cone penetration experiments and simulations as shown in Fig. 1a. In the calibration experiments, resistive forces are measured when the calibration cone penetrates into wet granular samples. This study uses two types of granular material with similar mean grain size and density, which are commonly used [22, 39]: glass beads (mean particle diameter = 0.2 mm and density = 2500 kg/m^3) as a near spherical and Toyoura sand (mean particle diameter = 0.2 mm and density = 2630 kg/m^3) as an angular particle material. The experiments are carried out as mentioned in the following. First, a wet sample is prepared by thoroughly mixing pure water and dry sample in an industrial mixer. Here, the amount of mass water content in wet granular samples is set as 5 %, based on the previous studies on glass beads [39] and sand [41]. These previous studies have reported that the penetration force or shear stress is almost saturated at a mass water content of around 5 %. These results might be caused by the change in the interstitial water status at moisture contents above 5 % and away from the pendular regime where the attraction force due to liquid bridge dominating the strength. Next, the wet sample is poured into a container and compacted by a

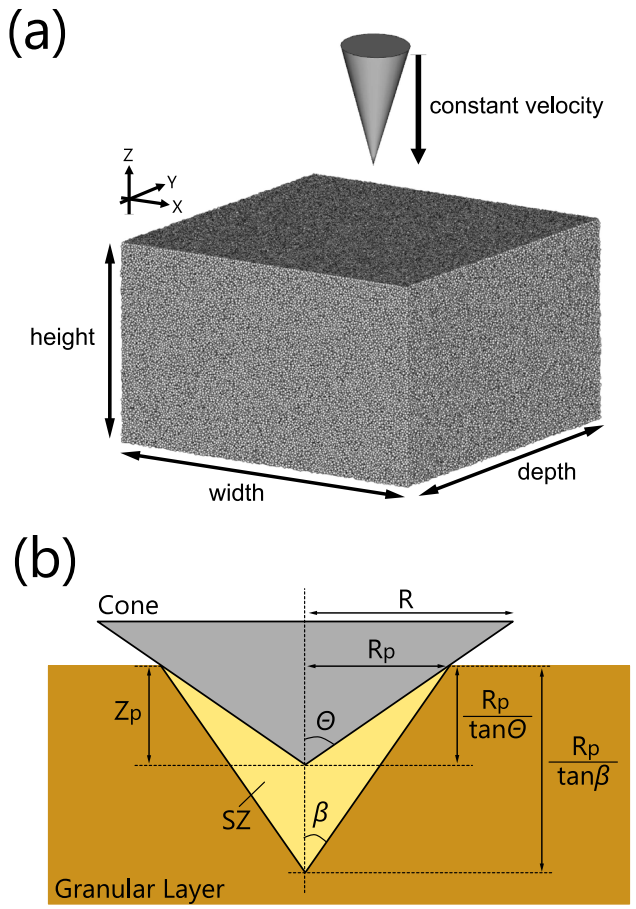

Fig. 1 **a** Schematic of setup for parameter calibration and cone penetration simulation. A cone penetrates along the z-direction into granular layer. **b** Schematic in cross-section view of the cone penetrating into granular layer. The cone shape is defined by Θ and R. z_p is the penetration depth to the cone-tip from the free surface of layer. R_p is the radius of the penetrated cone. A conical SZ with a tip angle β is formed in front of the cone. Using R_p, the penetration heights of the cone and SZ are $\frac{R_p}{\tan\Theta}$ and $\frac{R_p}{\tan\beta}$, respectively

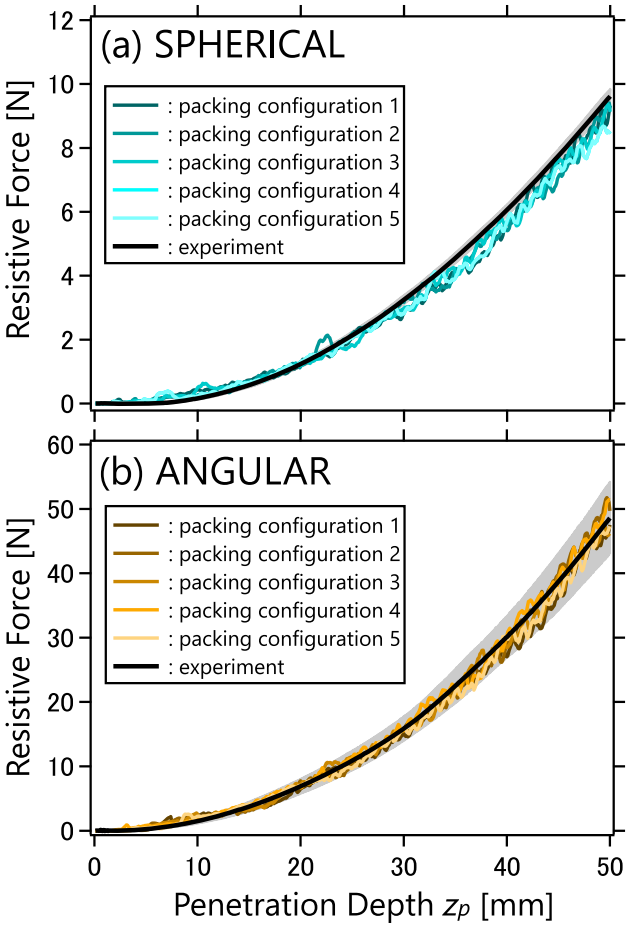

Fig. 2 Calibration results of the resistive force for **a** SPHERICAL and **b** ANGULAR. The horizontal axis is z_p, and the vertical axis is the resistive force in linear–linear scale. Colored lines indicate the results of DEM simulations with different packing configurations. The black lines indicate mean resistive force computed from twelve experiments for glass beads and nine experiments for Toyoura sand, respectively. The gray zones represent the region of standard deviation of the experiments

vibratory rammer. As a result, ψ after compaction are 0.57 for glass beads and 0.55 for Toyoura sand, respectively. Finally, the resistive force is measured by vertically penetrating the calibration cone into the wet granular layer. The calibration cone is made of aluminum with tip angle Θ = 15 deg and radius R = 28.6 mm as shown in the definition in Fig. 1b, which is the same dimensions as those commercially available for the Japanese Geotechnical Society Standards 1431: Method for portable cone penetration test (JGS-1431). The penetration velocity of 10 mm/s recommended by the JGS-1431 is used. The values of F_{wet} obtained from above calibration experiments are shown as black lines within Fig. 2a and b for glass bead and Toyoura sand, respectively.

In the simulations for DEM parameter calibration, first of all, simulation space is provided for calculating particles and cone-shaped intruder. The dimensions of simulation space are 200 mm in width and depth, and 180 mm in height. The edge of width (x-axis) and depth (y-axis) directions are set as periodic boundaries as in Roth [36]. In this setup, particles moving to coordinates below 0 mm or above 200 mm appear from the opposite boundary. In the height (z-axis) direction, the fixed flat floor is set at the bottom of layer (z = 0 mm) to prevent particles from falling. This floor is set to the same parameters as the particles to minimize the wall effect. Next, a large number of particles are generated in the space to create the granular layer of Fig. 1a. Here, the initial position of each particle during particle generation is determined using pseudo-random numbers. Generated particles in the space freely fall by gravity and form a granular layer. After packing, μ_{gg}, χ and C are, respectively, set to the corresponding experimental conditions, and then, the granular layer is

fully relaxed. After relaxation, particles presenting above 180 mm in height are removed, and a granular layer with a flat free surface is finally created, as shown in Fig. 1a. Subsequently, a cone of same dimensions to that used in the experiment (Θ = 15 deg and R = 28.6 mm) is positioned with their central axis aligned with the center of layer and penetrated into the granular layer. Comparing the experimental calibration data with the resistive force applied to the cone during penetration, μ_{gg}, μ_{og}, χ, and C are adjusted, respectively, to match both.

Here, supplementary explanations and assumptions for calibrating DEM parameters are provided. The particle diameter d is larger than that used in the experiments in order to reduce computational costs. With regard to particle size, Miyai et al and Paume et al [30, 34] have numerically and experimentally investigated the effect of particle size, and reported that there is little effect to F_{dry} when the particles are sufficiently smaller than the intruder. Thus, this study set the mean diameter to 2 mm ($\ll$ the diameter of calibration cone = 28.6 mm), which is about ten times larger than actual glass beads or Toyoura sand. For size distribution of particles, the three different size particles ($d_1 = 1.7$ mm, $d_2 = 2.0$ mm, and $d_3 = 2.3$ mm) are mixed in 1:2:1 ratio to avoid particle crystallization [14]. The density ρ_g, Poisson ratio v, and e of the particles are assumed constant for both granular materials to simplify calibrations. For ρ_g, the value of glass beads ($\rho_g = 2500$ kg/m^3) is used. For v and e, the values ($v = 0.25$ and $e = 0.9$) are used from the previous studies [21, 30] reproducing glass beads in DEM. For intruder density ρ_o, the value of aluminum ($\rho_g = 2700$ kg/m^3) is used. The value of ρ_o is required for calculations in LIGGGHTS, but this value has almost no influence when the intruder penetrates with constant speed, as in this study. For Young's modulus E of particles, values are adjusted to match experimental results using a value as low as possible to allow for a larger time step. This is because Miyai et al [30]; Kobayakawa et al [21]; and Roth [36] have already reported that DEM simulation can reproduce particle behaviors even when it is smaller than the Young's modulus of the actual particles. For timestep Δt, it is set from Rayleigh wave speed as in Thornton [43]. According to Otsubo et al [33], a value of 0.2–0.4 times the Rayleigh time $T_R = \frac{\pi d_2 \sqrt{2(1+v)\rho_g/E}}{2(0.1631v+0.8766)}$ should be used as Δt. In this study, it is set as $\Delta t = 4.0 \times 10^{-6}$ s from $T_R \sim 3.0 \times 10^{-5}$ s. In fact, anomalous particle behaviors are not observed in all simulations setting by $\Delta t = 4.0 \times 10^{-6}$ s. For the penetration velocity, Seguin et al [38] and Roth [36] have reported that F_{dry} does not change when the penetration velocity is less than the quasi-static velocity $\sqrt{4r^*g}$. In this study, the quasi-static velocity is $\sqrt{4r^*g} = 200$ mm/s. In consequence, this study sets the penetration velocity to 50 mm/s, which is about five times larger than experiments. Furthermore, this study also confirms no change in F_{dry} at penetration velocities of 10 mm/s and 50 mm/s.

Under the calibration setup and these assumptions, the resistive forces due to cone penetration are calibrated to match the experimental data. The calibration results are shown in Fig. 2 and Table 1. In addition, to match the simulations with the experimental data, ψ need to be set as 0.60 for glass beads and 0.58 for Toyoura sand. As the DEM parameters are different from physical properties of the glass beads and Toyoura sand in the calibration experiments, this study designates the parameter sets calibrated with glass beads and Toyoura sand as SPHERICAL and ANGULAR, respectively. In Table 1, the values of $C = 4.0 \times 10^2$ Pa for SPHERICAL and $C = 2.1 \times 10^3$ Pa for ANGULAR, respectively, correspond to calibration results matched to experimental data for 5 % mass moisture content. Furthermore, in this study, simulations are also carried out with different pseudo-random numbers used for particle generation in order to verify the effect of the initial particle configuration in the granular layer on F_{wet} during cone penetration. Specifically, this study calculates F_{wet} with five different initial particle configurations of granular layers with different pseudo-random numbers as shown by colored lines in Fig. 2. It is obvious from Fig. 2 that calibrated DEM parameter sets, SPHERICAL and ANGULAR, are able to reproduce the F_{wet} obtained in the calibration experiments, with little influence of the initial particle configurations.

2.3 Cone penetration simulation

The effects of cone-tip angle and liquid-bridge force on resistive forces are investigated by vertically penetrating a cone into a granular layer at a constant velocity. The setup for cone penetration simulation is basically same as calibration. However, the dimensions of granular layer are changed to 300 mm in width and depth because larger cones are used than the calibrations case, as described below. By comparing several conditions in advance, this study sets these width and depth to reduce the effect of boundary conditions and computational costs. This study uses two parameter sets obtained in the previous section, SPHERICAL and ANGULAR in Table 1, for the parameters required in the DEM simulations. With regard to the packing fraction, although its effect on the resistive force is observed during calibration, it is ignored in this study and set as $\psi = 0.60$ for both particle types. To archive $\psi = 0.60$, the specific values of DEM parameters ($\mu_{gg} = 0.30$, $\chi = 0$, and $C = 0$ Pa) are set when particles

Table 1 DEM parameter list

Material	SPHERICAL	ANGULAR
Parameter	Value	
Young's modulus E [Pa]	1.0×10^8	1.0×10^9
Poisson ratio v	0.25	0.25
Friction coefficient μ_{gg} (particle–particle)	0.31	0.70
Friction coefficient μ_{og} (intruder–particle)	0.27	0.30
Shape parameter χ	0.04	0.30
Particle diameter d_1, d_2, d_3 [mm]	1.7, 2.0, 2.3	1.7, 2.0, 2.3
Particle mixing ratio $d_1 : d_2 : d_3$	1:2:1	1:2:1
Particle density ρ_g [kg/m^3]	2.5×10^3	2.5×10^3
Intruder density ρ_o [kg/m^3]	2.7×10^3	2.7×10^3
Timestep Δt [s]	4.0×10^{-6}	4.0×10^{-6}
Coefficient of restitution e	0.90	0.90
Attraction stress parameter C [Pa]	0, 9.6	0, 49
	96, 4.0×10^2	4.9×10^2, 2.1×10^3

are generated. These particles fall due to gravity and pile up to form the layer. After this particle-packing procedure, the DEM parameters of SPHERICAL or ANGULAR are set and the granular layer relaxes. On this parameter setting, C is varied to investigate the effect of liquid-bridge force on penetration resistive forces. In this study, four values of C in total for each granular type are examined; the four values are, respectively, equivalent to 5 % mass water content used for the calibration (maximum value of C for each type in Table 1), the dry condition ($C = 0$ Pa), and two values existing between dry conditions to 5 % mass water content.

This study uses five cones with different tip angle Θ to investigate the effect of cone-tip angle on penetration resistive forces. Specific values of (Θ, R) employed are (15 deg, 28.6 mm), (30 deg, 28.6 mm), (45 deg, 42.9 mm), (60 deg, 42.9 mm), and (75 deg, 42.9 mm), respectively. The cone radii are set to twice and three times the values of the calibration cone. When Θ is increased with the same radius, the blunt cone is considerably smaller in volume than the one with an sharp angle. To ensure sufficient penetration volume, the radius of blunt cones (Θ = 45, 60, and 75 deg) is increased in this study. As shown in Fig. 1b, penetration depth z_p is defined as the depth to the cone-tip from the initial free surface level of granular layer. Simulations are performed until the cone is completely buried in granular layer (i.e., penetrated cone radius $R_p = z_p \tan \Theta$ reaches R shown in Fig. 1b).

Finally, in this study, one simulation is carried out per each simulation condition (a combination of cone shape, granular type, and attraction stress). This is because the initial particle configuration comprising the granular layer does not affect the penetration resistive force as shown in Fig. 2.

3 Results and discussion

3.1 Effect of cone-tip angle

First, the results of cone penetration simulations are compared with the MALT to discuss the effect of the cone-tip angle on F_{dry}. To compute F_{dry} from the MALT, V_p and K_ϕ must be estimated in addition to ρ_g and ψ. The volume of a penetrated cone is defined as $V_p = \frac{1}{3}\pi z_p^3 \tan^2 \Theta$. On the other hand, K_ϕ is computed from ϕ for granular material according to Eq. (1) derived by Kang et al [17]. As Kang et al [17] have used, this study uses angles of repose as ϕ. Specifically, sand piles for SPHERICAL and ANGULAR are developed through DEM simulation as shown in Fig. 3. Thereby, this study obtained the angles of repose, $\phi = 21$ deg for SPHERICAL and $\phi = 30$ deg for ANGULAR, respectively. Using these ϕ values and Eq. (1), K_ϕ is determined as $K_\phi = 11.7$ for SPHERICAL and $K_\phi = 35.2$ for ANGULAR, respectively. The comparisons of F_{dry} computed by Eq. (1) and the simulation results are shown in Fig. 4.

In Fig. 4, the simulation results of F_{dry} show proportional to the cube of z_p ($F_{dry} \propto V_p \propto z_p^3$). This relationship between F_{dry} and z_p is qualitatively consistent with the MALT (red dashed lines in Fig. 4). However, for blunter tip angles, simulation results deviate quantitatively from

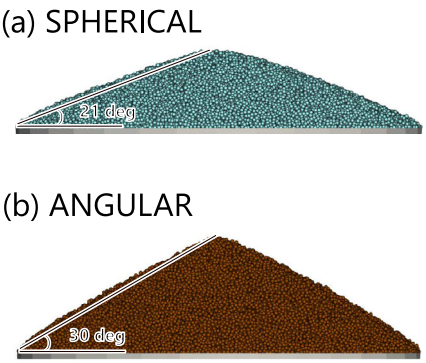

Fig. 3 Sand piles of **a** SPHERICAL and **b** ANGULAR calculated by DEM simulations. The bottom is made of a 200 mm diameter disk. The angle of repose is obtained using the height of sand piles and the radius of the bottom base. Angles of repose are $\phi = 21$ deg for SPHERICAL and $\phi = 30$ deg for ANGULAR, respectively

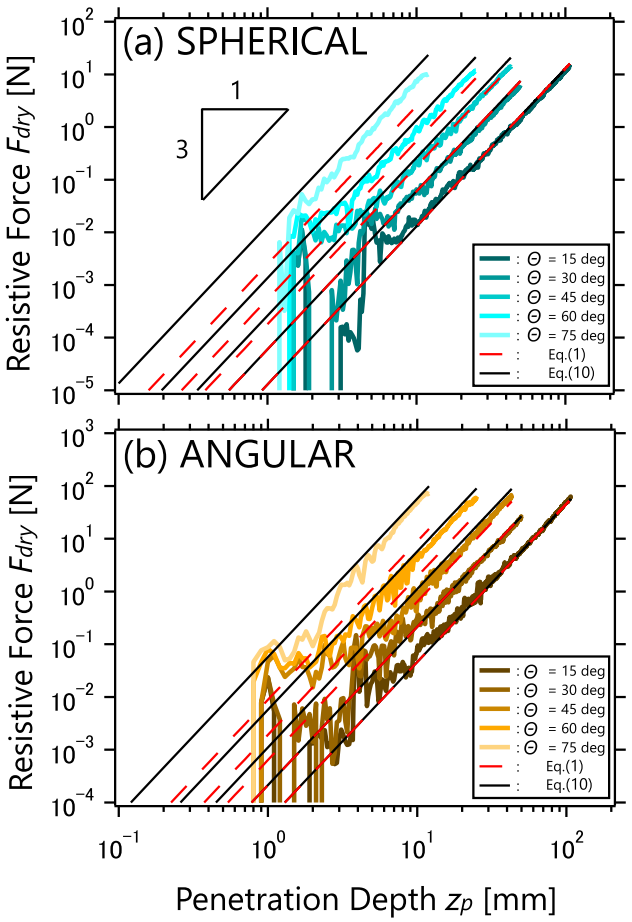

Fig. 4 Relationship between F_{dry} and z_p for **a** SPHERICAL and **b** ANGULAR. The horizontal axis is z_p, and the vertical axis is F_{dry} in log–log scale. Colored lines indicate results of the DEM simulation with various cone-tip angles Θ. The red dashed lines are F_{dry} computed by Eq. (1). The black solid lines are F_{dry} computed by Eq. (10)

MALT. To identify deviations between the simulation results and the MALT with regard to Θ, the ratio D_{MALT} is defined as follows and evaluated for each Θ:

$$D_{MALT} = \frac{F_{dry}}{K_\phi \rho_g \psi g V_p}. \tag{7}$$

The computed D_{MALT} values from the last 80 % of the time series of penetration data for each Θ are shown by hollow markers in Fig. 5. If there is no effect of cone-tip angle, D_{MALT} should be almost constant regardless of Θ. However, Fig. 5 reveals that D_{MALT} represented by Eq. (7) increases rapidly when Θ is larger than around 45 deg. This result indicates that the blunter the cone-tip angle, the more F_{dry} deviates from the MALT. Specifically, the difference between simulation results and MALT is up to five times ($D_{MALT} \simeq 5$) for $\Theta = 75$ deg with ANGULAR.

For the limit of blunt angles (i.e., the flat-bottom cylinder), Aguilar and Goldman [1]; Kang et al [17]; and Feng et al [11] have confirmed that a sudden increase in F_{dry} occurs in the extremely shallow penetration depth (about 0.1 times the intruder's diameter). This sudden increase in F_{dry} during shallow penetration is caused by a conical stagnation zone (SZ) where granular particles move as a rigid body in front of the intruder. In fact, [1]; Tovar-Valencia Ruben D. et al [44] have confirmed the formation of SZ in front of cylinder penetration through experimental analysis of particle motion. To consider the effect of this SZ on F_{dry}, Kang et al [17] and Feng et al [11], who have proposed the MALT, have shown that this rapid increase in F_{dry} can not be directly explained by the MALT. To solve this disagreement, these previous studies have taken into

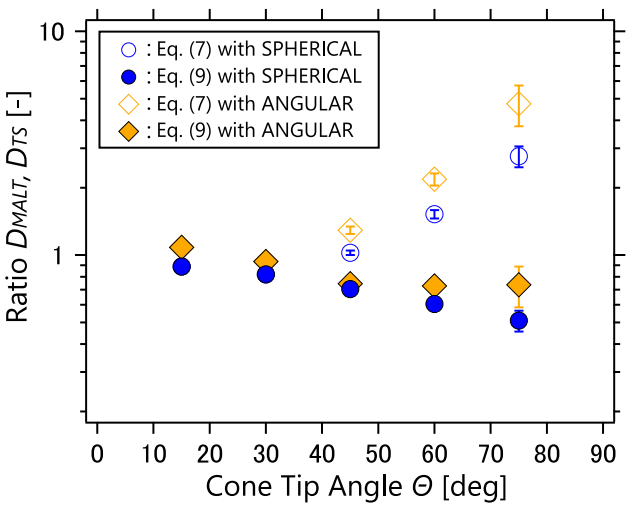

Fig. 5 Variation of D_{MALT} and D_{TS} with respect to Θ. The vertical axis is D_{MALT} and D_{TS}, and the horizontal axis is Θ in log–linear scale. Colors and markers indicate differences for SPHERICAL and ANGULAR, respectively. Hollow and solid markers, respectively, represent the ratio of simulation results to the model in dry condition for Eqs. (7) and (9). The error bars indicate the standard deviation

account the rapid increase for F_{dry} in the early stages by adding constant values at the moment when the cylinder penetrated into the granular surface ($z_p = 0$). Aguilar and Goldman [1] have explained the increase in F_{dry} by the gradual development of the SZ and its virtual mass. The principal difference between these previous studies and this study is the use of cones whose cross-sectional area varies with z_p. Considering this difference, it can be assumed that the SZ formed in front of the blunt cone gradually grows itself as the cross-sectional area of the penetrated cone increases. Taking into account this SZ growth, larger F_{dry} than that computed by MALT can be explained.

Here, this study investigates the effect of the SZ on F_{dry} by examining the particle velocity and stress distributions around the penetrated cone. Figure 6 shows the particle velocity and stress distributions for ANGULAR in the final states of cone penetration with different tip angles. The tip angle of SZ is defined as $\beta = \frac{\pi}{4} - \frac{\phi}{2}$, as in Meyerhof [27] and Koumoto et al [24]. Using the ϕ values obtained from sand pile simulations, the values of β are, respectively, calculated as $\beta = 34.5$ deg from $\phi = 21$ deg for SPHERICAL and $\beta = 30$ deg from $\phi = 30$ deg for ANGULAR. In Fig. 6, the following two results with regard to SZ are revealed: (1) SZ forms with a magnitude proportional to the penetration cross-section. In addition, from the time-series data on the same cone, this study also confirms that SZ gradually grows itself as the cross-sectional area increases. (2) The particle velocity and stress distributions in front of the cone vary depending on Θ. In the case of cone-tips sharper than SZ ($\Theta = 15$ and 30 deg), there are few particles moving in the penetration direction and no stress chains in front of the cone. By contrast, in the case of a blunt cone ($\Theta = 45$, 60, and 75 deg), there are particles moving in the penetration direction and stress chains in front of the cone. Furthermore, the distribution of moving particles and stress chains in front of the blunt cone is concentrated within the region of SZ. These results suggest the importance of SZ for explaining large F_{dry} due to the virtual mass in blunt cones as well as in Aguilar and Goldman [1].

Accordingly, the correction factor $f(\Theta)$ is considered when virtual mass is assumed in front of the cone. For a sharper cone than SZ ($\Theta \leq \beta$), correction is not required, i.e., $f(\Theta) = 1$. For a blunter cone than SZ ($\Theta > \beta$), the positional relationship between the cone and the SZ is illustrated as in Fig. 1b, based on the results of Fig. 6. Then, assuming that the volume of the SZ is the practical penetration volume, $f(\Theta)$ equals the ratio of the height of the cone to the SZ. The penetration heights of both are $\frac{R_p}{\tan\Theta}$ and $\frac{R_p}{\tan\beta}$ respectively, as shown in Fig. 1b. Hence, $f(\Theta)$ is defined as follows:

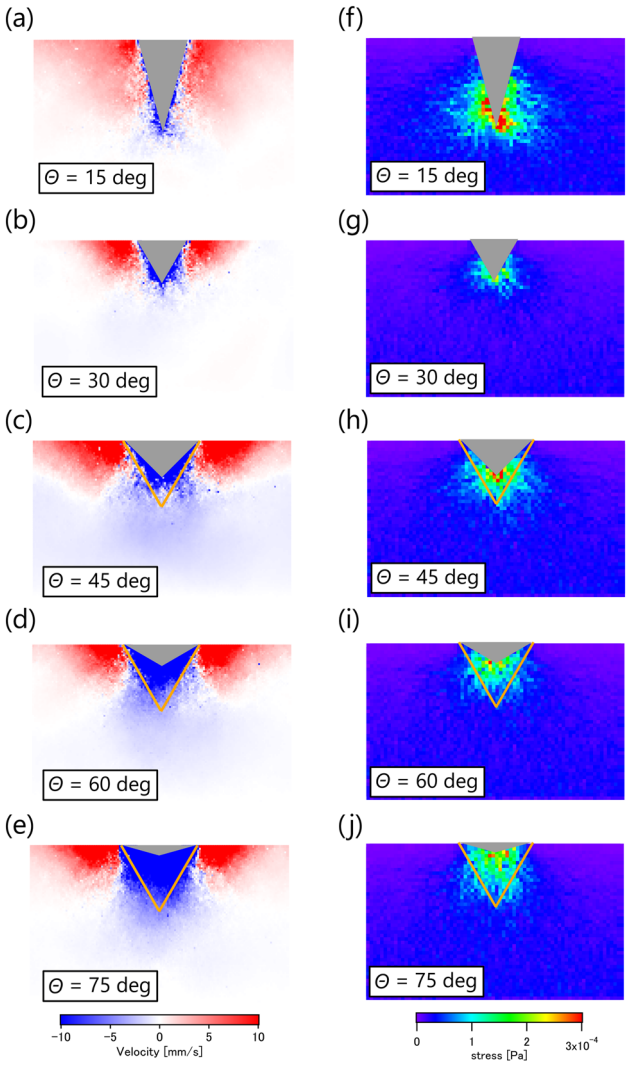

Fig. 6 **a–e** Particle velocity field in z-direction for ANGULAR on cross-section view. As represented by the color bar, red and blue indicate positive and negative particle velocities in z-direction, respectively. **f–j** Stress distributions on cross-section view for ANGULAR visualized from the stress on the particle. As the color bar indicates, the higher the stress on the particle, the warmer the color. The orange lines show the shape of the SZ at tip angle $\beta = 30$ deg for ANGULAR expected from the penetrated cone radius

$$f(\Theta) = \begin{cases} \dfrac{\tan\Theta}{\tan\beta} & : \text{if } \Theta > \beta, \\ 1 & : \text{if } \Theta \leq \beta. \end{cases} \tag{8}$$

Using Eq. (8), the ratio of the simulation results to the model is modified as follows:

$$D_{TS} = \frac{F_{dry}}{f(\Theta) K_\phi \rho_g \psi g V_p}. \tag{9}$$

The Θ dependence of D_{TS} is shown by solid markers in Fig. 5. The data used to compute the mean and standard deviation are the same as in D_{MALT}. D_{TS} in Fig. 5 has a

slight decreasing trend with respect to Θ, but it is close to unity than MALT, even for blunt cones. Specifically, the difference between simulation results and the proposed model is reduced to up to twice ($D_{TS} \simeq 0.5$) for $\Theta = 75$ deg with SPHERICAL.

Therefore, in the case of blunt cones, the increase in F_{dry} has been caused by the virtual mass due to the difference between the SZ region and the penetrated cone volume. Accounting for this increase, this study proposes the modification of MALT as follows:

$$F_{dry}(z_p) = f(\Theta) K_\phi \rho_g \psi g V_p(z_p). \tag{10}$$

A comparison between the simulation results and Eq. (10) is described as black solid lines in Fig. 4. In Fig. 4, the quantitative agreement can be confirmed.

3.2 Effect of liquid-bridge force

Next, the effect of liquid-bridge force on penetration resistive force is discussed. In this study, the basic equations are first derived based on the slip line field theory from the Mohr–Coulomb's yield criterion including the cohesion term as in Koumoto et al [24]. Furthermore, F_{wet} is modeled in a similar way to Kang et al [17] while taking into account the effect of SZ due to the cone-tip angle. The details of the derivation are explained in Appendix A. As a result, the following equation for F_{wet} is obtained:

$$F_{wet}(z_p) = f(\Theta) K_\phi \rho_g \psi g V_p(z_p) + K_c C' S_p(z_p), \tag{11}$$

where C' is the bulk cohesive stress. This study calls Eq. (11) as the WG-MALT model. The coefficient of cohesion-derived force K_c in Eq. (11) is expressed using K_ϕ in Eq. (1) as follows:

$$K_c = \left(2 \frac{1+\sin\phi}{1-\sin\phi} e^{\pi \tan\phi} \int_0^1 \eta A(\eta, \phi) d\eta - 2 \int_0^1 \eta d\eta \right)$$
$$\cot\phi = \left(K_\phi - 2 \int_0^1 \eta d\eta \right) \cot\phi. \tag{12}$$

In addition, the penetration volume V_p and the cross-sectional area S_p of a penetrated cone in Eq. (11) are, respectively, expressed by using z_p as follows:

$$V_p(z_p) = \frac{1}{3} \pi z_p^3 \tan^2 \Theta,$$
$$S_p(z_p) = \pi z_p^2 \tan^2 \Theta. \tag{13}$$

Here, Eq. (12) indicates that K_c also depends only on ϕ as in K_ϕ. From Eqs. (1) and (12), the variations of K_ϕ and K_c with regard to ϕ are computed as in Fig. 7. To determine these coefficients for each material, ϕ in wet granular materials is required. In this study, ϕ is assumed to be unchanged by liquid-bridge force since Pierrat et al [29, 35] have reported that ϕ does not change in wet granular materias. Thereby, the values of K_c are, respectively, determined as $K_c = 27.7$ from $\phi = 21$ deg for SPHERICAL and $K_c = 70.4$ from $\phi = 30$ deg for ANGULAR. Using these equations and the coefficient values, the WG-MALT can compute F_{wet}.

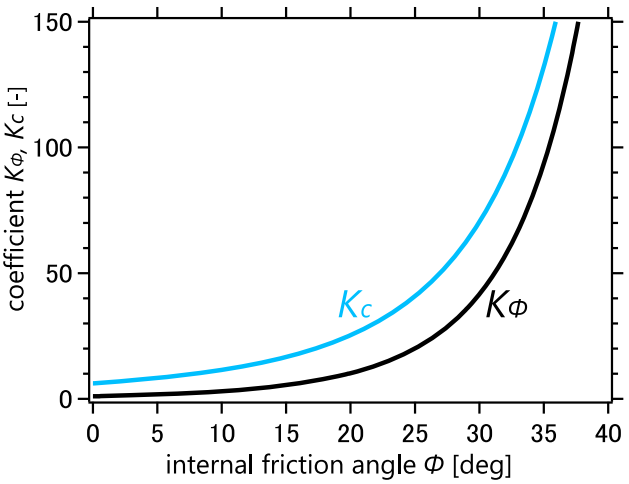

Fig. 7 Variations with respect to ϕ of the coefficients K_ϕ and K_c computed by Eq. (12). Black solid line indicates the coefficient of buoyancy-like force K_ϕ. Blue solid line indicates the coefficient of cohesion-derived force K_c

Having been discussed in the previous section, the first term on the right-hand side in Eq. (11) is the same as in Eq. (10). Therefore, this study focuses on the second term on the right-hand side of Eq. (11), indicating the liquid-bridge-derived resistive force (F_C), and discusses its applicability. To estimate F_C from the simulation results, this study defines that F_C is the difference by subtracting F_{dry} from F_{wet}, thus, $F_C(z_p) \equiv F_{wet}(z_p) - F_{dry}(z_p)$. Comparison of F_C under each simulation condition and model cohesive force $K_c C S_p$ is shown in Fig. 8. Based on the geometric relationship in the Mohr–Coulomb's yield criterion and the attraction stress applied between the particles in Eq. (6), this study assumes $C' = C$ and uses it for computing F_{wet}. In Fig. 8, the following two results with regard to F_C are revealed: (1) As C becomes large, F_C also increases as in Sharpe et al [39]; Bagheri et al [4]; and Cheng et al [10]; (2) F_C increases proportionally to the square of z_p ($F_C \propto S_p \propto z_p^2$). To clarify quantitative deviations between the simulation results and the model cohesive force, this study defines the ratio D_{LB} as follows:

$$D_{LB} = \frac{F_C}{K_c C S_p}. \tag{14}$$

The variations of D_{LB} for each C and Θ is shown in Fig. 9. For computing values of mean and standard deviation, as in D_{MALT} and D_{TS}, the last 80 % of the time series of

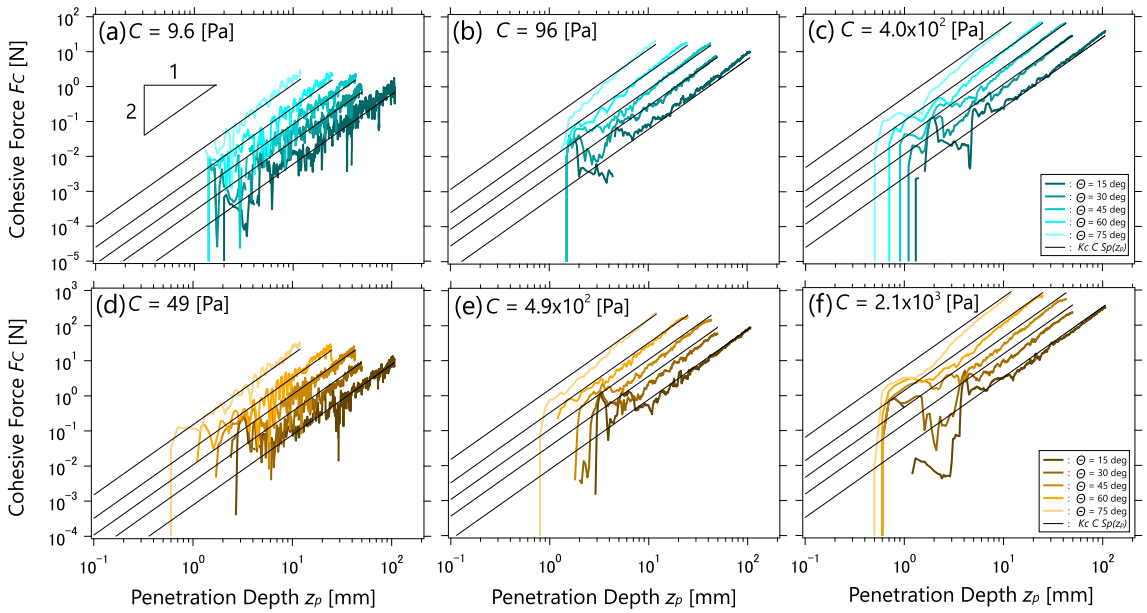

Fig. 8 Relationship between F_C and z_p for **a–c** SPHERICAL and for **d–f** ANGULAR. The horizontal axis is z_p, and the vertical axis is F_C in log–log scale. Colored lines indicate the DEM simulation results with differences in Θ. The solid black lines are model cohesive forces computed from $K_c C S_p(z_p)$

penetration data is used for each C and Θ. Figure 9 shows that D_{LB} is close to unity over the entire Θ range although it has a decrease trend as C increases. Moreover, this result indicates that the difference between the derived model and the simulation results is up to twice ($D_{LB} \simeq 2$) for $\Theta = 15$ deg and $C = 9.6$ Pa with SPHERICAL, even when standard deviations are taken into account. This dependence of the cohesion-derived resistive force on the tip angle differs from the previous studies [12, 23], which have found that clay-derived penetration resistance depends on the cone-tip angle. However, sufficient data are not available for detail comparison at present. For this reason, this study claims that resistive force derived from liquid-bridge (or that can be reproduced by the cohesive bond model used in this study) is not affected by cone-tip shape.

From the above, it is found that the second term on the right-hand side of Eq. (11) quantitatively explains F_C. Besides, F_{dry} is explained by Eq. (10), which takes into account the effect of Θ. Hence, F_{wet} can be explained by assuming superposition of these terms. Here, Fig. 10 compares the simulation results for F_{wet} with the value computed by Eq. (11). In Fig. 10, F_{wet} obtained from the simulation varies between two and three in the slope of the power depending on the magnitude of C and also with Θ. Moreover, these values computed by Eq. (11) indicate good agreement under all simulation conditions. Therefore, WG-MALT model (Eq. 11) can quantitatively compute resistive forces at shallow penetration into dry and wet granular materials, taking into account the effect of the cone-tip angle and liquid-bridge forces between particles.

3.3 Limitations and future directions

In the calibration of DEM parameters, this study uses the experimentally obtained resistive forces into the wet granular layers. In this method, the parameters are always adjusted to include the effects of cohesion due to water content. Consequently, it is not strictly guaranteed that the simulation reproduces the resistive force in a dry condition ($C = 0$ Pa). In other words, the validity of the parameters determining the physical properties of dry granular materials such as μ_{gg} and χ has not been adequately assessed. Moreover, it is noted that the calibration is only carried out for $\Theta = 15$ deg. Hence, cone penetration simulations with different cone-tip might deviate from the experimental resistive forces. The simulation results indicate differences from the proposed model for blunt cones, but these differences could be reduced by improving calibration accuracy. Therefore, it is helpful for model improvement to calibrate the DEM parameter sets through experimental resistive forces under various water content and cone shape conditions.

When calculating penetration resistive force through the proposed model, this study uses ϕ obtained from the simulation and the values of C set in the simulation. The validity of using ϕ in MALT has been confirmed by experiments [17]. On the other hand, with regard to the newly introduced cohesion parameter in the proposed model, this study confirms only the consistency with the value of C used in the simulation. However, it is unclear how it corresponds to the cohesion of wet granular

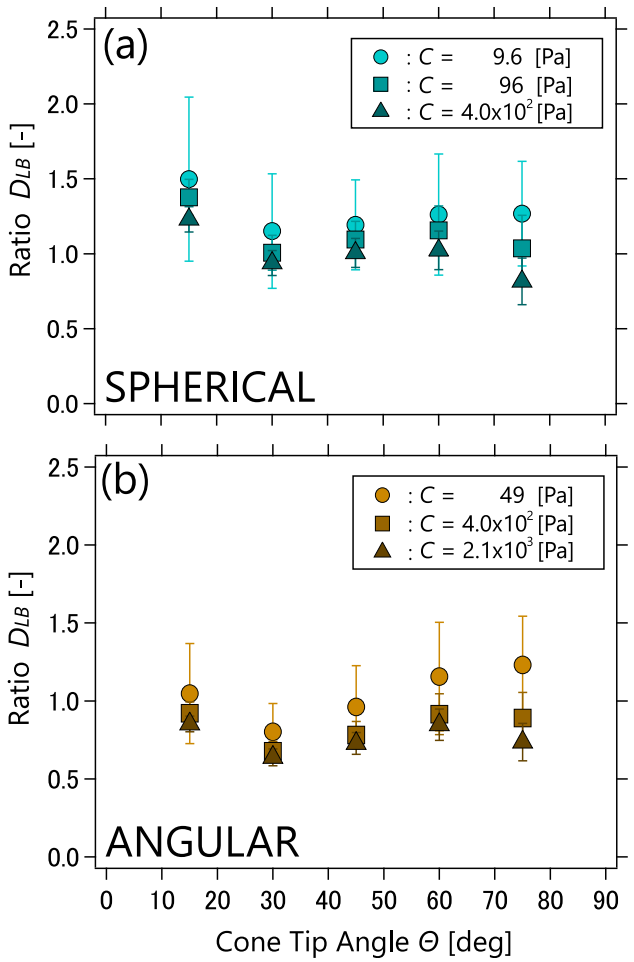

Fig. 9 Variation of D_{LB} with respect to Θ for **a** SPHERICAL and **b** ANGULAR. The vertical axis is D_{LB}, and the horizontal axis is Θ in linear–linear scale. Colors and markers indicate, respectively, differences of C. The error bars indicate the standard deviation

materials measured in experiments. Accordingly, it would be important in application to verify the cohesion parameter in the simulation and the proposed model comparing with the cohesion of granular layer measured from triaxial compression tests and other element tests.

In addition to the limitations described above, there are the following several issues in the application of WG-MALT in actual soils. The first is to investigate the validity of WG-MALT through experiment. This is obviously important for applications. Second, the effect of parameters not considered in this study should be investigated to clarify the applicability of WG-MALT. Specifically, these are packing fraction and particle size distribution of the soil materials, friction coefficient between particle and an intruder, intruder shape, and penetration velocity. As some of these parameters are difficult to control systematically in experiments, simulation studies should be useful.

4 Conclusion

This study investigated the effects of cone-tip angle and liquid-bridge force due to water content on the resistive force during shallow cone penetration into dry and wet granular layers at quasi-static velocities. The effect of cone-tip angle on the F_{dry} was investigated by comparing DEM simulation results in dry conditions ($C = 0$ Pa) with the MALT model (Eq. 1). When the cone had a shaper tip than the SZ, F_{dry} can be computed by MALT. On the other hand, when the cone had blunter tip than the SZ, F_{dry} was up to five times greater than the MALT compute. Through the analysis of the particle velocity field and stress distributions in the fully cone penetrated states, this study revealed that the increase in F_{dry} on blunt cone was caused by the SZ which gradually grows during the cone penetration pushing the surrounding particles (Fig. 6). In addition, for blunt cones, it was shown that the difference between the model and F_{dry} can be reduced by up to twice by considering the correction factor $f(\Theta)$ to the MALT, which takes into account the growing volume of the SZ (Eq. 10 and Fig. 4). With regard to the effect of liquid-bridge force on the resistive force, the model equations which consider effects of cohesion stress in the Mohr–Coulomb's yield criterion (Eqs. 11–13) were first derived theoretically. Next, the applicability of the derived model was confirmed by comparing the model computations with the DEM simulation results for the liquid-bridge-derived resistive force F_C (Fig. 8). As a result, the model was also able to estimate F_C with a maximum difference in a factor of two of the simulation results. From the above results, Eq. (11) can be regarded as the improved MALT model, named WG-MALT in this study, which takes into account the effect of the cone-tip angle by $f(\Theta)$ and also deals with the effect of liquid-bridge force. Besides, the applicability of the WG-MALT was confirmed by comparing it with F_{wet} in wet granular layers at various Θ and C through DEM simulations (Fig. 10). Namely, the WG-MALT improved the previous MALT by considering the effects of the cone-tip angle and liquid-bridge force between particles, which can be crucial issues in actual applications in many fields including Geotechnical Engineering, Planetary Science, Biology, and Terramechanics.

Appendix A: Theoretical analysis for resistive force into the wet granular layer

In this section, the characteristic curves and the basic equations of F_{wet} in wet granular layer are analyzed from the slip line field theory by assuming the Mohr–Coulomb's yield criterion including cohesive stress as in Koumoto

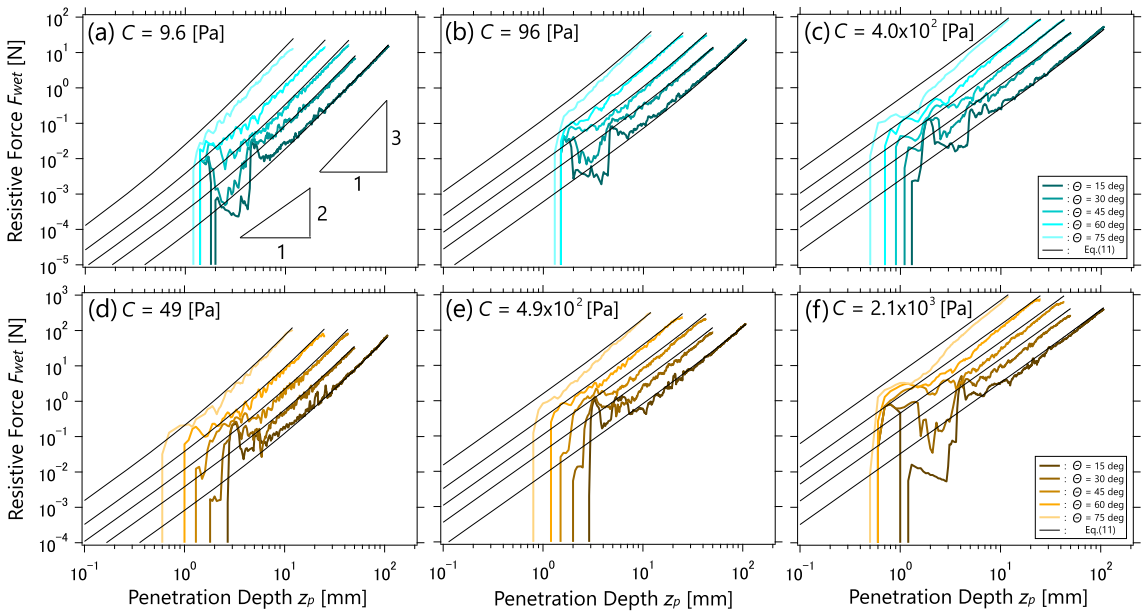

Fig. 10 Relationship between F_{wet} and z_p for **a**–**c** SPHERICAL and for **d**–**f** ANGULAR. The horizontal axis is z_p, and the vertical axis is F_{wet} in log–log scale. Colored lines indicate the DEM simulation results with differences in Θ. The solid black lines are penetration resistive forces computed by Eq. (11)

et al [24]. It then extends the MALT to a form applicable to a cone penetrating against wet granular layer by means of a similar way to Kang et al [17].

When a granular layer is considered as a continuum, the two-dimensional stress components on an infinitesimal triangle element in a granular layer is as shown in Fig. 11a. In Fig. 11a, σ_1 and σ_3 orthogonal to each other are the major and minor principal stresses, respectively. Here, σ_1 is inclined counterclockwise α degrees from the r-axis. τ_{rz}, σ_r, and σ_z are shear stress, normal stress in r-axis and z-axis direction, respectively. Each stress in wet granular layer is represented by Mohr's stress circle in Fig. 11b. Moreover, on the plastic equilibrium state, a straight line (failure envelope) is tangent to the Mohr's stress circle as shown in Fig. 11b. This yield criterion in which stresses satisfy the state in Fig. 11b is called as the Mohr–Coulomb yield criterion, and the following relationships are established [42]:

$$\begin{cases} \tau = C' + \sigma \tan\phi, \\ \dfrac{\sigma_1 - \sigma_3}{2} = \dfrac{\sigma_1 + \sigma_3}{2}\sin\phi + C'\cos\phi, \end{cases} \tag{A1}$$

where τ and σ represent the local shear and normal stress, respectively; and C' is the bulk cohesive stress.

In cylindrical coordinates (r, θ, z), $\tau_{\theta r} = \tau_{\theta z} = 0$ is assumed due to axial symmetry. The azimuthal stress σ_θ is considered as the intermediate principal stress σ_2 in addition to σ_1 and σ_3. Moreover, assuming $\sigma_2 (= \sigma_\theta)$ to be equivalent to σ_3 as in Kang et al [17], the problem in cylindrical coordinates is eventuated to the analysis on the plastic equilibrium state in the r-z plane shown in Fig. 11a. From the stress relationship in Fig. 11b, Eq. (A1), and defining the mean principal stress $\sigma_0 \equiv (\sigma_1 + \sigma_3)/2$ in r-z plane, the stress components are described as follows:

$$\begin{aligned} \sigma_r &= \sigma_0(1 + \sin\phi\cos 2\alpha) + C'\cos\phi\cos 2\alpha, \\ \sigma_z &= \sigma_0(1 - \sin\phi\cos 2\alpha) - C'\cos\phi\cos 2\alpha, \\ \tau_{rz} &= (\sigma_0\sin\phi + C'\cos\phi)\sin 2\alpha, \\ \sigma_\theta &= \sigma_0(1 - \sin\phi) - C'\cos\phi. \end{aligned} \tag{A2}$$

Neglecting the effect of the granular own weight, the stress components satisfy following the equilibrium equations:

$$\begin{cases} \dfrac{\partial\sigma_r}{\partial r} + \dfrac{\partial\tau_{rz}}{\partial z} + \dfrac{\sigma_r - \sigma_\theta}{r} = 0 \\ \dfrac{\partial\tau_{rz}}{\partial r} + \dfrac{\partial\sigma_z}{\partial z} + \dfrac{\tau_{rz}}{r} = 0 \end{cases} \tag{A3}$$

Substituting Eqs. (A2) into Eqs. (A3), the following equation is obtained:

$$\mathbf{X}\cdot\frac{\partial\mathbf{u}}{\partial r} + \mathbf{Y}\cdot\frac{\partial\mathbf{u}}{\partial z} = \mathbf{q}, \tag{A4}$$

with $\mathbf{u} = \begin{pmatrix} \sigma_0 \\ \alpha \end{pmatrix}$, and

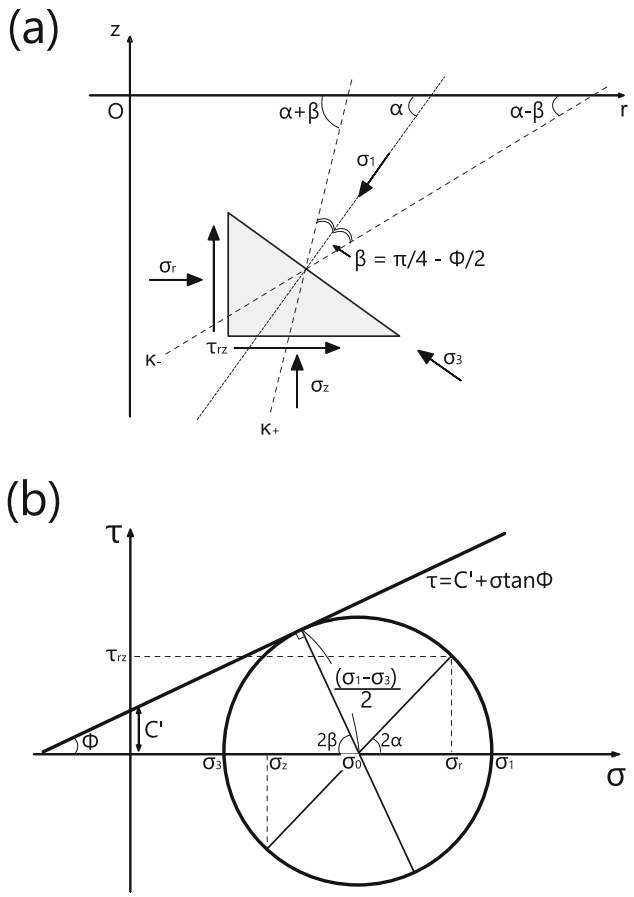

Fig. 11 **a** Schematic of stress state applied to a triangular element in r-z plane. The major and minor principal stresses, σ_1 and σ_3, are positive in the direction of the arrow. κ_+ and κ_- are, respectively, shown as dotted lines. **b** Mohr's stress circle which satisfies the yield criterion Eq. (A1). The radius and center of the circle are $\frac{\sigma_1-\sigma_3}{2}$ and σ_0, respectively. Each stress in **a** is shown as a point on the circle

$$\mathbf{X} = \begin{pmatrix} 1+\sin\phi\cos 2\alpha & -2\sin 2\alpha(\sigma_0\sin\phi + C'\cos\phi) \\ \sin\phi\sin 2\alpha & 2\cos 2\alpha(\sigma_0\sin\phi + C'\cos\phi) \end{pmatrix},$$

$$\mathbf{Y} = \begin{pmatrix} \sin\phi\sin 2\alpha & 2\cos 2\alpha(\sigma_0\sin\phi + C'\cos\phi) \\ 1-\sin\phi\cos 2\alpha & 2\sin 2\alpha(\sigma_0\sin\phi + C'\cos\phi) \end{pmatrix},$$

$$\mathbf{q} = -\frac{1}{r}(\sigma_0\sin\phi + C'\cos\phi)\begin{pmatrix} 1+\cos 2\alpha \\ \sin 2\alpha \end{pmatrix}.$$

The equation for the stress field is first-order linear simultaneous partial differential equations of hyperbolic type. These equations can be solved using the method of characteristics, and then, characteristic curves are described as follows [17, 24]:

$$\kappa_\pm \equiv \frac{dz}{dr} = \tan(\alpha \pm \beta) \quad ; \quad \beta = \frac{\pi}{4} - \frac{\phi}{2}, \tag{A5}$$

where the two characteristic curves are denoted by κ_+ and κ_-, respectively. The angle between κ_+ and κ_- is always 2β at any point in the r-z plane. The locations of κ_+ and κ_- for σ_1 and its angle α in the r-z plane are presented in Fig. 11a. Referring to these characteristic curves, the following basic equations are obtained [24]:

$$d\sigma_0 = -(\sigma_0\tan\phi + C')\left(\pm 2d\alpha + \frac{\cos\phi}{r}dr \pm \frac{1-\sin\phi}{r}dz\right). \tag{A6}$$

Here κ_+ and κ_- are mathematically allowed to have discontinuities at the stress value or the stress direction in the direction across Eq. (A6). In other words, the characteristic curve can be regarded as a slip line since the discontinuity of the stress across the curve is maintained only along the characteristic curve. Therefore, the stress state on each slip line in the plastic region can be determined from Eq. (A6) by giving the stress boundary conditions.

Next, assuming the situation that the cone penetrates at z_p from the initial free surface level of a granular layer as shown in Fig. 12, the resistive force applied to a cone of the penetrated radius R_p is considered. In Fig. 12, the penetrating cone situations differ from the case of a cylinder in two points, the appearance of the SZ and the concept of pressure due to gravity. With regard to SZ, as it is clear from Fig. 6, whether the SZ occurs in front of the cone (Fig. 12b) or not (Fig. 12a) is determined by depending on the relationship between the tip angle of the cone and the SZ. With regard to the gravity-derived pressure for cones, it is necessary to treat SZ differently for cylinders. In the case of cylinders, the bottom of the SZ is the same as the flat tip and still coincides with z_p. In contrast, in the case of cones, the bottom of the SZ is always on the free surface of a granular layer as shown in Fig. 12. Thus, in this study, the pressure is adjusted to fit penetration resistive force obtained from Kang et al [17] and Fig. 4. In particular, this study assumes that a virtual uniform pressure $P = f(\Theta)\rho_g\psi g z_p$ proportional to the tip position of the cone or SZ acts on the free surface of the granular layer. Here, it is assumed that P increases hydrostatically in proportion to z_p as with general granular layer [15]. The correction factor $f(\Theta)$ is same definition as in Eq. (8). Furthermore, for simplicity, it is also assumed that the shape of the free surface remains flat after the penetration. Regarding the validity of this assumption, Kobayashi et al [22] have reported that even a model assuming a flat surface can estimate the resistive force of penetrating cone in experiments.

On the above situations, shear stresses on boundaries AB and BD can be neglected since these stresses are sufficiently small relative to the normal forces on the penetrating cone. Around the cone, a cylindrically symmetric stress state consists of three regions as in cylinder [17, 22, 24], as shown in Fig. 12. First region is a triangular

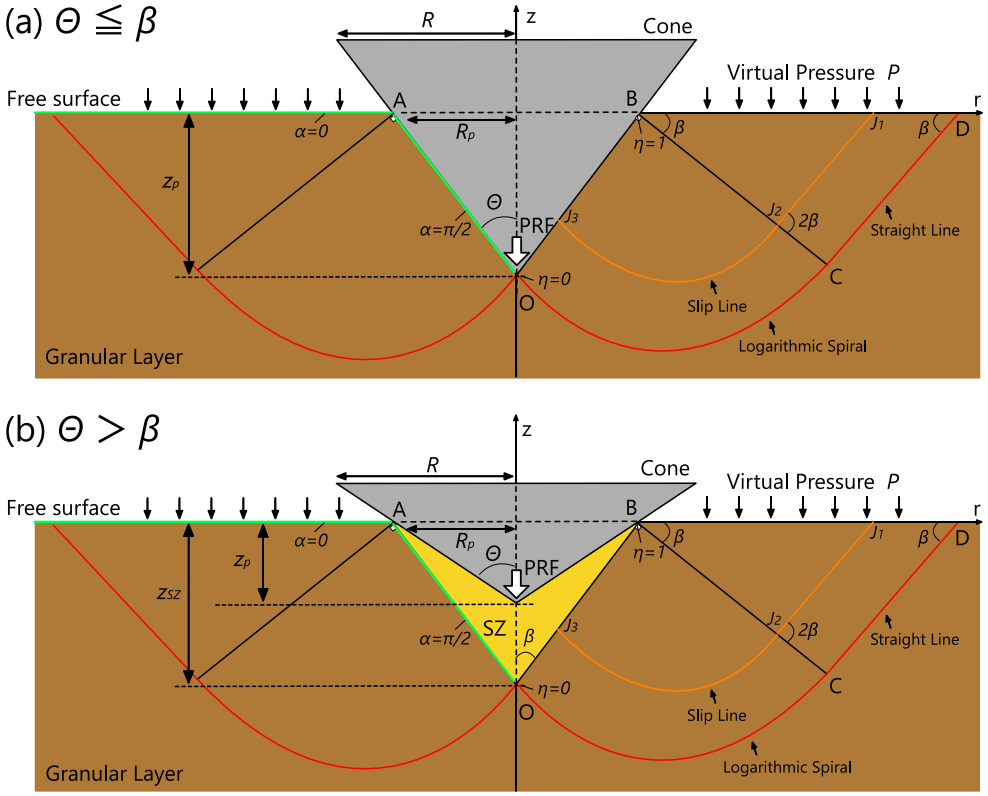

Fig. 12 Schematic in cross-section view of stress state around cone at z_p in the cases of **a** $\Theta \leq \beta$ and **b** $\Theta > \beta$. SZ with tip angle β is formed in front of the cone when the cone-tip angle is blunter than that of SZ. Uniform virtual pressure P acts on the free surface level of a granular layer. κ_+ and κ_- are represented by red and black lines, respectively. κ_+ consists of logarithmic spirals and straight lines. The orange line is one of the κ_+, and the positions of the intersection of the curve with the line segments BD, BC, and BO are indicated by the points J_1, J_2, and J_3, respectively. The green lines represent the angle α of σ_1, $\alpha = \pi/2$ on the boundary of the SZ and $\alpha = 0$ at the same depth as the base of the penetrated cone

zone AOB, as the cone itself or SZ; second region is a fan-shaped transition zone OBC bounded by a logarithmic spiral with maximum displacement angle $\pi/2$ centered at point B; and third region is a triangular passive zone BCD.

In addition, the cone itself or the SZ behaves as a boundary, and slip lines (characteristic curves) occur from these surface. The slip line along the characteristic curve moves in a logarithmic spiral in the second region and in a straight line with angle β in the third region as shown in Fig. 12. The (r, z) coordinates of the intersection points J_1, J_2, and J_3 of any slip line and each segment BD, BC, and BO, respectively, are as follows:

$$J_1 = R_p\left(1 + \frac{2(1-\eta)}{\tan\beta}e^{\frac{\pi}{2}\tan\phi}, 0\right),$$
$$J_2 = R_p\left(1 + \frac{1-\eta}{\tan\beta}e^{\frac{\pi}{2}\tan\phi}, -(1-\eta)e^{\frac{\pi}{2}\tan\phi}\right), \tag{A7}$$
$$J_3 = R_p\left(\eta, -\frac{\eta}{\tan\beta}\right),$$

where $\eta = \overline{OJ_3}/\overline{OB} \in [0, 1]$ is defined as shown in Fig. 12.

The points (r, z) along logarithmic spiral between J_2 and J_3 are as follows:

$$r = R_p\left(1 + \frac{(1-\eta)\sin(\lambda-\beta)}{\sin\beta}e^{\lambda\tan\phi}\right),$$
$$z = -R_p\left(\frac{(1-\eta)\cos(\lambda-\beta)}{\sin\beta}e^{\lambda\tan\phi}\right), \tag{A8}$$

where λ represents the displacement angle from the segment BO centered at point B and $\lambda \in [0, \pi/2]$. By integrating the characteristic curve of Eq. (A6) along the slip line J_1, J_2, and J_3, and defining

$$Z(\eta,\phi) \equiv \int_{r_3}^{r_2}\frac{dz}{r}$$
$$= \int_0^{\frac{\pi}{2}}\frac{(\eta-1)e^{\lambda\tan\varphi}\cos(\lambda+\beta)}{\cos\varphi[\sin\beta + (1-\eta)e^{\lambda\tan\varphi}\sin(\lambda-\beta)]}d\lambda, \tag{A9}$$
$$A(\eta,\phi) \equiv \left(\frac{r_1^{1+\tan^2\beta}}{r_2^{\tan^2\beta}r_3}\right)^{\sin\phi}e^{\sin\phi\tan\beta Z(\eta,\phi)},$$

the following equation is obtained:

$$\sigma_0(\eta)_{J3}\tan\phi + C' = (\sigma_0(\eta)_{J1}\tan\phi + C')e^{\pi\tan\phi}A(\eta,\phi). \tag{A10}$$

From the z-axis directional balancing equation in Eq. (A2), $\sigma_0(\eta)_{J1} = \frac{P+C'\cos\phi}{1-\sin\phi}$ for $\alpha = 0$ and $\sigma_z(\eta) = \sigma_0(\eta)_{J3}(1+\sin\phi) + C'\cos\phi$ for $\alpha = \pi/2$ are, respectively, calculated. Using these expressions and Eq. (A10), σ_z along the surface OB on the cone itself or the SZ is obtained as follows:

$$\sigma_z(\eta) = \frac{1+\sin\phi}{1-\sin\phi}A(\eta,\phi)e^{\pi\tan\phi}P + \left(\frac{1+\sin\phi}{1-\sin\phi}A(\eta,\phi)e^{\pi\tan\phi} - 1\right)C'\cot\phi. \tag{A11}$$

Defining the coefficients K_ϕ and K_c which depend only on ϕ as Eqs. (1) and (12), and then by surface integrating with respect to σ_z applied to the cone itself or the SZ using Eq. (A11), F_{wet} can be derived as follows:

$$F_{wet}(z_p) = f(\Theta)K_\phi\rho_g\psi g z_p\pi R_p^2 + K_c C'\pi R_p^2. \tag{A12}$$

From the above equation, F_{wet} is expressed as the sum of the force proportional to the penetration volume due to inter-particle friction [8, 17] and the force proportional to the penetration area due to cohesion stress in a granular layer [12, 23]. Here, Eq. (11) is derived from replacing the part corresponding to the penetrated volume of the cylinder in Eq. (A12) by $V_p(z_p) = z_p\pi R_p^2$ as in [17] and the part corresponding to the penetrated cross-sectional area by $S_p(z_p) = \pi R_p^2$. Although V_p is assumed as a cylinder in the transformation of Eq. (A12) to Eq. (11), Kang et al [17] have reported that Eq. (11) can estimate penetration resistive force on shapes other than cylinders by using V_p along the intruder shape. In fact, using Eq. (13) for the penetration volume and the cross-sectional area of the penetrated cone, Eq. (11) can explain resistive forces of penetrating cone in both dry and wet granular layers as shown in Figs. 4 and 10.

Acknowledgements The authors would like to acknowledge the financial support from Komatsu Ltd. This work was supported by JSPS KAKENHI Grant Number JP24H00196.

Funding Open Access funding provided by Osaka University.

Data availability All data in this study are available from the corresponding author on reasonable request.

References

1. Aguilar J, Goldman DI (2016) Robophysical study of jumping dynamics on granular media. Nat Phys 12(3):278–283
2. Ai J, Chen JF, Rotter JM et al (2011) Assessment of rolling resistance models in discrete element simulations. Powder Technol 206(3):269–282
3. Askari H, Kamrin K (2016) Intrusion rheology in grains and other flowable materials. Nat Mater 15(12):1274–1279
4. Bagheri H, Jayanetti V, Burch HR et al (2023) Mechanics of bipedal and quadrupedal locomotion on dry and wet granular media. J Field Robot 40(2):161–172
5. Ballouz RL, Walsh KJ, Sánchez P et al (2021) Modified granular impact force laws for the OSIRIS-REx touchdown on the surface of asteroid (101955) bennu. Mon Not R Astron Soc 507(4):5087–5105
6. Berger R, Kloss C, Kohlmeyer A et al (2015) Hybrid parallelization of the LIGGGHTS open-source DEM code. Powder Technol 278:234–247
7. Bergmann PJ, Berry DS (2021) How head shape and substrate particle size affect fossorial locomotion in lizards. J Exp Biol 224(11):jeb242244
8. Brzinski TA III, Mayor P, Durian DJ (2013) Depth-dependent resistance of granular media to vertical penetration. Phys Rev Lett 111(16):168002
9. Cheng B, Yu Y, Baoyin H (2018) Collision-based understanding of the force law in granular impact dynamics. Phys Rev E 98(1):012901
10. Cheng B, Asphaug E, Yu Y et al (2023) Measuring the mechanical properties of small body regolith layers using a granular penetrometer. Astrodynamics 7(1):15–29
11. Feng Y, Blumenfeld R, Liu C (2019) Support of modified archimedes' law theory in granular media. Soft Matter 15(14):3008–3017
12. Houlsby GT (1982) Theoretical analysis of the fall cone test. Géotechnique 32(2):111–118
13. Hunt OM, O'Hara KB, Chen Y et al (2023) Numerical and physical modeling of the effect of the cone apex angle on the penetration resistance in Coarse-Grained soils. Int J Geomech 23(2):04022273
14. Iikawa N, Bandi MM, Katsuragi H (2016) Sensitivity of granular force chain orientation to Disorder-Induced metastable relaxation. Phys Rev Lett 116(12):128001
15. Iikawa N, Bandi MM, Katsuragi H (2018) Force-chain evolution in a two-dimensional granular packing compacted by vertical tappings. Phys Rev E 97(3):032901
16. Jiang M, Shen Z, Wang J (2015) A novel three-dimensional contact model for granulates incorporating rolling and twisting resistances. Comput Geotech 65:147–163
17. Kang W, Feng Y, Liu C et al (2018) Archimedes' law explains penetration of solids into granular media. Nat Commun 9(1):1101
18. Katsuragi H (2016) Physics of soft impact and cratering. Springer
19. Katsuragi H, Durian DJ (2007) Unified force law for granular impact cratering. Nat Phys 3:420–423
20. Kloss C, Goniva C (2011) LIGGGHTS-open source discrete element simulations of granular materials based on lammps.

Supplemental Proceedings: Materials Fabrication, Properties, Characterization, and Modeling 2
21. Kobayakawa M, Miyai S, Tsuji T et al (2020) Interaction between dry granular materials and an inclined plate (comparison between large-scale DEM simulation and three-dimensional wedge model). J Terramech 90:3–10
22. Kobayashi T, Fukagawa R (2002) Matsuura T (2002) Theoretical analysis of cpt and a proposal of an idea for estimating strength parameters. Doboku Gakkai Ronbunshu 708:117–131
23. Koumoto T, Houlsby GT (2001) Theory and practice of the fall cone test. Géotechnique 51(8):701–712
24. Koumoto T, Meyerhof GG, Sastry VVRN (1985) Ultimate bearing capacity of axially loaded piles based on three-dimensional analysis. Comput Geotech 1(3):181–194
25. Li C, Zhang T, Goldman DI (2013) A terradynamics of legged locomotion on granular media. Science 339(6126):1408–1412
26. Martinez A, Dejong J, Akin I et al (2022) Bio-inspired geotechnical engineering: principles, current work, opportunities and challenges. Géotechnique 72(8):687–705
27. Meyerhof GG (1951) The ultimate bearing capacity of foudations. Géotechnique 2(4):301–332
28. Mishra AK, Tramacere F, Guarino R et al (2018) A study on plant root apex morphology as a model for soft robots moving in soil. PLoS One 13(6):e0197411
29. Mitarai N, Nori F (2006) Wet granular materials. Adv Phys 55(1–2):1–45
30. Miyai S, Kobayakawa M, Tsuji T et al (2019) Influence of particle size on vertical plate penetration into dense cohesionless granular materials (large-scale DEM simulation using real particle size). Granular Matter 21(4):105
31. Obermayr M, Vrettos C, Eberhard P et al (2014) A discrete element model and its experimental validation for the prediction of draft forces in cohesive soil. J Terramech 53:93–104
32. Okubo F, Katsuragi H (2022) Impact drag force exerted on a projectile penetrating into a hierarchical granular bed. Astron Astrophys 664:A147
33. Otsubo M, O'Sullivan C, Shire T (2017) Empirical assessment of the critical time increment in explicit particulate discrete element method simulations. Comput Geotech 86:67–79
34. Paume V, Aussillous P, Pouliquen O (2023) Finite size effects during the penetration of objects in a granular medium. Soft Matter 20(1):245–254
35. Pierrat P, Agrawal DK, Caram HS (1998) Effect of moisture on the yield locus of granular materials: theory of shift. Powder Technol 99(3):220–227
36. Roth LK (2021) Constant speed penetration into granular materials: drag forces from the quasistatic to inertial regime. Granular Matter 23(3):54
37. Ruck JG, Wilson CG, Shipley T et al (2024) Downslope weakening of soil revealed by a rapid robotic rheometer. Geophys Res Lett 51(1):e2023GL106468
38. Seguin A, Bertho Y, Martinez F et al (2013) Experimental velocity fields and forces for a cylinder penetrating into a granular medium. Phys Rev E 87(1):012201
39. Sharpe SS, Kuckuk R, Goldman DI (2015) Controlled preparation of wet granular media reveals limits to lizard burial ability. Phys Biol 12(4):046009
40. Suzuki H, Kawakami H, Kobayashi T et al (2023) Extended terramechanics model for machine-soil interaction: representation of change in the ground shape and property via cellular automata. Soil Tillage Res 226:105578
41. Takita H, Sumita I (2013) Low-velocity impact cratering experiments in a wet sand target. Phys Rev E 88(2):022203
42. Terzaghi K (1943) Theoretical soil mechanics. John Wiley & Sons, Incorporated
43. Thornton C (2000) Numerical simulations of deviatoric shear deformation of granular media. Géotechnique 50(1):43–53
44. Tovar-Valencia Ruben D, Ayda Galvis-Castro, Rodrigo Salgado et al (2021) Effect of base geometry on the resistance of model piles in sand. J Geotech Geoenviron Eng 147(3):04020180
45. Tsuji T, Nakagawa Y, Matsumoto N et al (2012) 3-D DEM simulation of cohesive soil-pushing behavior by bulldozer blade. J Terramech 49(1):37–47
46. Tsuji T, Matsui Y, Nakagawa Y et al (2013) DEM study on the interaction between wet cohesive granular materials and tools. AIP Conf Proc 1542(1):947–950